Quantitative evaluation of the lunar seismic scattering and comparison between the Earth, Mars, and the Moon

K. Onodera[1,2,3], T. Kawamura[2], S. Tanaka[4], Y. Ishihara[5], and T. Maeda[6]

[1]Earthquake Research Institute, The University of Tokyo, Tokyo, Japan.

[2]Université Paris Cité, Institut de Physique du Globe de Paris, CNRS, Paris, France.

[3]The Graduate University for Advanced Studies, SOKENDAI, Kanagawa, Japan.

[4]Institute of Space and Astronautical Science, Japan Aerospace Exploration Agency, Kanagawa, Japan.

[5]JAXA Space Exploration Center (JSEC), Japan Aerospace Exploration Agency, Kanagawa, Japan.

[6]Graduate School of Science and Technology, Hirosaki University, Aomori, Japan.

Corresponding author: Keisuke Onodera (onodera@eri.u-tokyo.ac.jp)

Key Points:

- Through full 3D seismic wave propagation simulation, we quantitatively evaluated the lunar seismic scattering properties.
- We found that a 10 km thick scattering layer with 10% velocity fluctuation well-reproduced the Apollo seismic observation.
- Our results show that the upper lunar crust is about ten times more heterogeneous than that of the Earth and Mars.

Abstract

The intense seismic scattering seen in Apollo lunar seismic data is one of the most characteristic features, making the seismic signals much different from those observed on the Earth. The scattering is considered to be attributed to subsurface heterogeneity. While the heterogeneous structure of the Moon holds the evolution and past geological activities, the detailed description remains an open issue. Here we present a new model of the subsurface heterogeneity within the upper lunar crust derived through a full 3D seismic wave propagation simulation. Our simulation successfully reproduced the Apollo seismic observations, leading to a significant update of the scattering properties of the Moon. The results showed that the scattering intensity of the Moon is about ten times higher than that of the heterogeneous region on the Earth. The quantified scattering parameters could give us a constraint on the surface evolution process on the Moon and enable the comparative study for answering a fundamental question of why the seismological features are different on various planetary bodies.

Plain Language Summary

In the past Apollo missions, several seismometers were installed on the nearside of the Moon and they brought us the first seismic records from an extraterrestrial body. The derived lunar seismic data surprised us because of their extremely long duration (1 – 2 hours) and spindle-shaped form, which were barely observed on Earth. These characteristics different from earthquakes are thought to reflect the subsurface heterogeneity. However, the inhomogeneous structure within the lunar crust is poorly constrained. To improve our knowledge of wave propagation on an extraterrestrial body, this study evaluated the subsurface heterogeneity through 3D seismic wave propagation simulation. After running some simulations under various structure settings, we found that a certain set of parameters well reproduced the Apollo seismic data, resulting in a new heterogenous structure of the Moon. The evaluated parameters were compared with those measured on the Earth and Mars, and we found that the Moon is more heterogeneous than others by about ten times. This kind of comparison makes it easier to interpret the observed seismic signals on each solid body. Also, it is useful to explain the differences in their surface evolution scenarios. We believe that our results contribute to further extending comparative planetology.

1 Introduction

The intensely scattered seismic waves with a long duration (1 – 2 hours) and ambiguous phase arrivals (e.g., P, S) are one of the characteristics observed in the Apollo lunar seismic data (Latham et al., 1970). According to the previous studies on Earth, it is considered that this feature is ascribed to the subsurface heterogeneities such as cracks, igneous intrusions, and faults (Sato et al., 2012 and references therein). While the intense scattering is the essence of the lunar seismic signals, its properties are poorly evaluated in a quantitative way. The past studies estimated the diffusivity and the intrinsic attenuation — the energy decay due to the absorption by medium — by fitting the energy decay part (Figure 1) and contributed to a better understanding of the long event duration seen in the Apollo data (Dainty and Toksöz, 1981). The problem was that their approach could not fully explain the energy growth part where the forward scattering effect is more dominant (Figure 1).

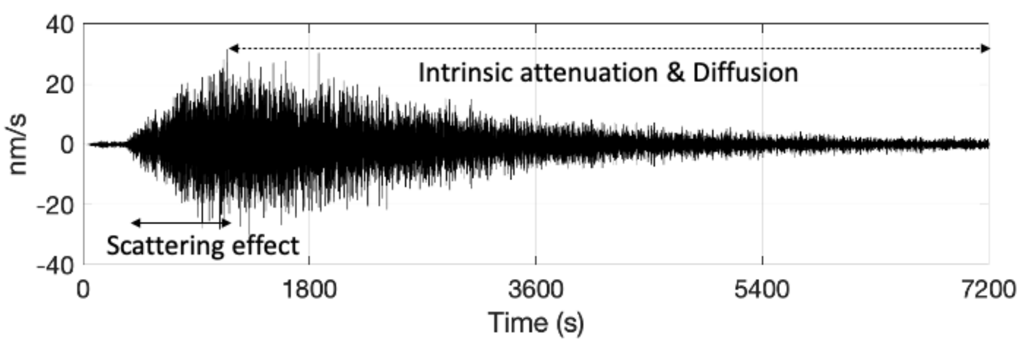

Figure 1. An example of a lunar seismic wave. The horizontal axis shows time in seconds and the vertical shows the velocity in nm/s. This is an impact-induced event recorded on July 17 in 1972 with the vertical component of the long-period seismometer installed at the Apollo 15 landing site. The waveform is bandpass filtered between 0.3 and 1.5 Hz. This event is estimated to have occurred about 3000 km away from the Apollo 15 station (Oberst, 1989).

Generally speaking, estimating the planetary interior using seismic waves relies on precise phase identifications (e.g., P, S arrivals). Yet, the extremely high scattering environment on the Moon makes it more challenging to pick up the phases, leading to considerable uncertainty in the resultant structure model (e.g., Garcia et al., 2019). Thus, it can be said that the scattering is an essential characteristic of the lunar seismic waves, whereas it is a most severe obstacle for the investigation of the internal structure. Moreover, the seismic data from Mars also show intensely scattered features (e.g., Lognonné et al., 2020;

Menina et al., 2021), implying that seismic scattering is not just a specific problem in lunar seismology but also a common problem in planetary seismology. Therefore, it is valuable to push forward our understanding of this topic for elucidating the nature of seismic wave propagation on extraterrestrial bodies.

In this study, by employing a more direct way than before, we quantitatively evaluated the lunar scattering properties, which have remained an open and severe issue since lunar seismology started. Here we present the updated scattering properties of the Moon derived through the first full 3D simulation of seismic wave propagation in lunar seismology. Our high spatiotemporal resolution simulation enabled us to directly compare the Apollo observation and synthetics at the same frequency range. Moreover, we successfully reproduced the first part of the coda within a reasonable parameter range, allowing us to evaluate the scattering attenuation factor quantitatively. Additionally, we compare our results with the Earth and Mars, and discuss why we observe different seismological features on each solid body. Since this kind of comparative study helps us infer how the evolution process differs among solid planetary bodies, we believe that our results not just contribute to deepening our understanding of the Moon but also pushing forward comparative planetology.

In the following sections, we present the fundamental idea about the 3D seismic wave propagation simulation and how to compare the simulated results with the observation. Then, we show the results and discuss the obtained fractured structure within the lunar crust together with the previously proposed models. Finally, we make a comparison between the Earth, Mars, and the Moon in terms of seismic scattering and intrinsic absorption.

2 Methodology

In modeling the lunar seismic scattering, we adopted a new approach. The previous works (e.g., Dainty and Toksöz, 1981; Gillet et al., 2017) inverted scattering and attenuation parameters such as scattering attenuation factor (Q_s) and intrinsic attenuation factor (Q_i) based on the radiative transfer theory, where it is considered how incidence wave loses the energy due to scattering media and how the shape of energy envelope varies depending on the intensity of heterogeneity (e.g., Sato et al., 2012). Under the intense heterogeneity, this approach works well to explain the decay coda, which strongly reflects the intrinsic attenuation — the energy absorption by medium. Whereas the theory is not fully capable of modeling the energy growth part (from the first arrival to the energy peak arrival: Figure 1), where the scattering effects are more dominant. To overcome this problem, we performed forward modeling with 3D seismic wave propagation simulation, including all possible scattering sources such as topographies and wave velocity fluctuation, so to speak, full 3D simulation. The idea is to perform wave propagation simulations under various settings and to find a set of parameters that can well-reproduce the observations. While such an approach was known to be the most straightforward way to evaluate the scattering environment, it was unrealistic to take this approach because it requires a vast amount of computational resources. Recently, accompanied by the significant progress in computational technology, it is now possible to perform the forward approach. In this study, utilizing one of the best supercomputers existing (Earth Simulator 4th generation of Japan Agency for Marine-Earth Science and Technology), we performed the first full 3D simulation in lunar seismology to constrain the scattering properties more directly. In this section, we summarize the key points of the numerical simulation.

2.1 Simulation code for 3D seismic wave propagation

We used the Open-source Seismic Wave Propagation Code (OpenSWPC) developed by Maeda et al. (2017), which is based on the finite difference method with heterogeneity, oceanic layer, and topography (HOT-FDM; Nakamura et al., 2012). The code enables us to include both lunar topographies and scattering media that are mandatory functionalities in this study. Another point is that we realized a stable computation up to 2 Hz, which covers the peak sensitivity frequency band of the Apollo long period (LP) seismometer (0.3 – 1.5 Hz), realizing the first direct comparison between the synthetics and the Apollo data at the same frequency range.

2.2 Reference events and work space

Since this work is the first attempt of full 3D simulation in this field, it is reasonable to start with the artificial impacts because of their well-constrained source locations, origin times, and impact parameters (e.g., kinetic energy, impact angle). Following Onodera et al. (2021) who performed 2D simulation of the lunar seismic wave propagation, we adopted two SIVB rocket booster impacts: Apollo 16 SIVB and Apollo 14 SIVB impacts recorded at Apollo 12 station (Figure 2a). The computational space for each event is shown in Figure 2b-c. The detailed configuration of the simulation is summarized in Text S1.

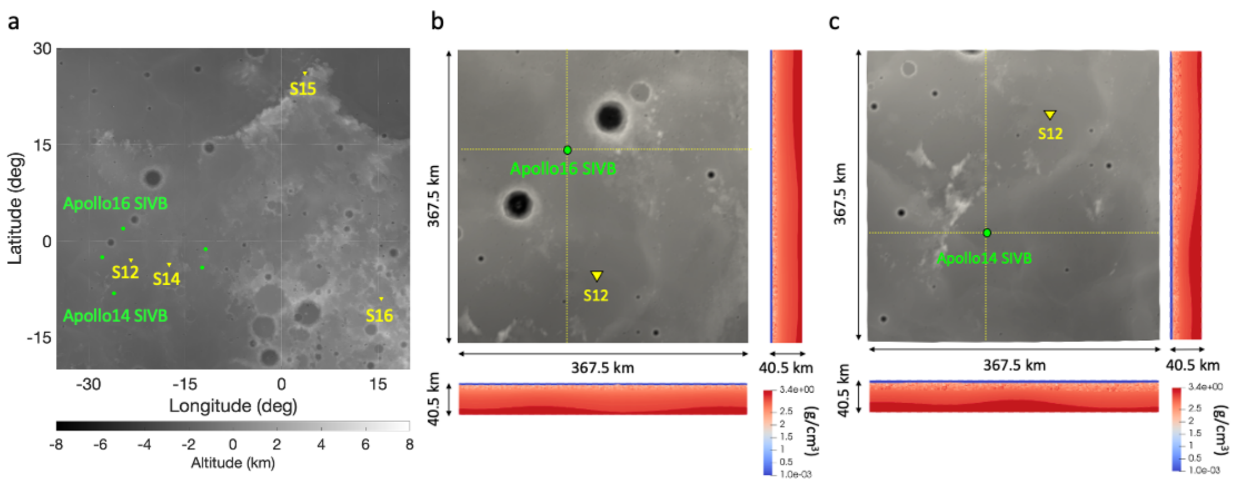

Figure 2. (a) Locations of Apollo SIVB impacts and Stations. The yellow inverse triangles show the locations of the Apollo seismometers and the green circles show the impact locations of the Apollo SIVB rocket boosters. The background is the digital elevation model (DEM) of the SELENE (Kaguya) laser altimeter (Araki et al., 2009). (b) Workspace for the 3D simulation of the Apollo 16 SIVB impact. The bottom and right-hand side panels display the cross-sections of E-W and N-S directions along with the yellow dotted lines. The grayscale corresponds to the surface topography (SLDEM2015; Barker et al., 2016) and the colored scale shows the density within the crust and mantle. The Moho boundary is inserted based on GRAIL crustal model by Wieczorek et al. (2013). Note that the first several km includes random media (i.e., the density fluctuation). (c) Workspace for the 3D simulation of the Apollo 14 SIVB impact. The color scales and each panel are the same as in (b).

2.3 Velocity structure

In constructing the velocity model, the gravity data from the Gravity Recovery and Interior Laboratory (GRAIL) mission and the measurements of Apollo returned samples were considered.

Regarding the density structure estimated from the GRAIL data, we used the density and porosity model provided by Besserer et al. (2014). Following their model, the density profile as a function of depth $\rho(z)$ can be written as:

$$\rho(z) = \rho_{surf} + \Delta\rho(1 - e^{-z/d}) \qquad (1)$$

where ρ_{surf} is the surface density, $\Delta\rho$ is the density contrast between fractured surface materials and unfractured bedrock, and d is the e-folding depth. At the Apollo 12 landing region, these parameters take the values of 2,308 kg/m^3, 786 kg/m^3, and 9.8 km, respectively. The porosity as a function of depth $\phi(z)$ can be expressed as:

$$\phi(z) = 1 - \rho(z)/\rho_0 \qquad (2)$$

where $\rho_0 = \rho_{surf} + \Delta\rho$. Substituting Equation 1 into Equation 2 gives us

$$\phi(z) = 1 - \frac{1}{\rho_{surf}+\Delta\rho}\left[\rho_{surf} + \Delta\rho(1 - e^{-\frac{z}{d}})\right]. \qquad (3)$$

In terms of the laboratory measurements, we referred an experimental work by Sondergeld et al. (1979). They constructed an empirical model of the compressional wave velocity $v_p(z)$ based on the measurements of the lunar anorthosite (Apollo sample: #60025, 174) like:

$$v_p(z) = \frac{v_{p0}}{\sqrt{1-\phi(z)}} \exp\left[\frac{(\phi(z)^2 - \xi)\phi(z)}{2(1-\phi(z))}\right] \qquad (4)$$

where v_{p0} (= 7.15 km/s) is the P-wave velocity extrapolated from high pressure to zero pressure based on the results by Mizutani and Osako (1974). ξ is an empirical constant and the value ranges from 2 to 24, covering almost all velocity structure models proposed by previous works (Besserer et al., 2014, Sondergeld et al., 1979). In other words, ξ=2 gives the upper limit of the P-wave velocity structure while ξ=24 does the lower limit. Combining Equation 3 with the empirical velocity structure by Sondergeld et al. (1979) results in the reference model used in the simulations. We employed ξ=7 based on the travel times computed for respective artificial impacts. See Text S2 and S3 for the determination of ξ parameter and additional information about topography model.

Figure 3a shows the constructed P-wave velocity model. The model consists of three parts: megaregolith (the fragmented structure due to meteoroid impacts), crust, and mantle from top to bottom. It is worth noting that the random media, whose thickness varies from 3.5 to 10 km in the simulation, are inserted in the megaregolith layer. We will explain the scattering layer in the next section. With regards to the V_P/V_S ratio, Lognonné et al. (2003) and Gagnepain-Beyneix et al. (2006) suggested that it could range from 1.7 to 2.0 for high fractured materials. Also, Garcia et al. (2011) employed 2.0 for the top low-velocity layer. In this study, following the previous results, the value in the scattering layer is assumed to be 2.0. Concerning the consolidated layer, $\sqrt{3}$ is given for V_P/V_S. The intrinsic Q used in the simulation was provided by combining the results by Nakamura and Koyama (1982), and Blanchette-Guertin et al. (2012) (Table S1).

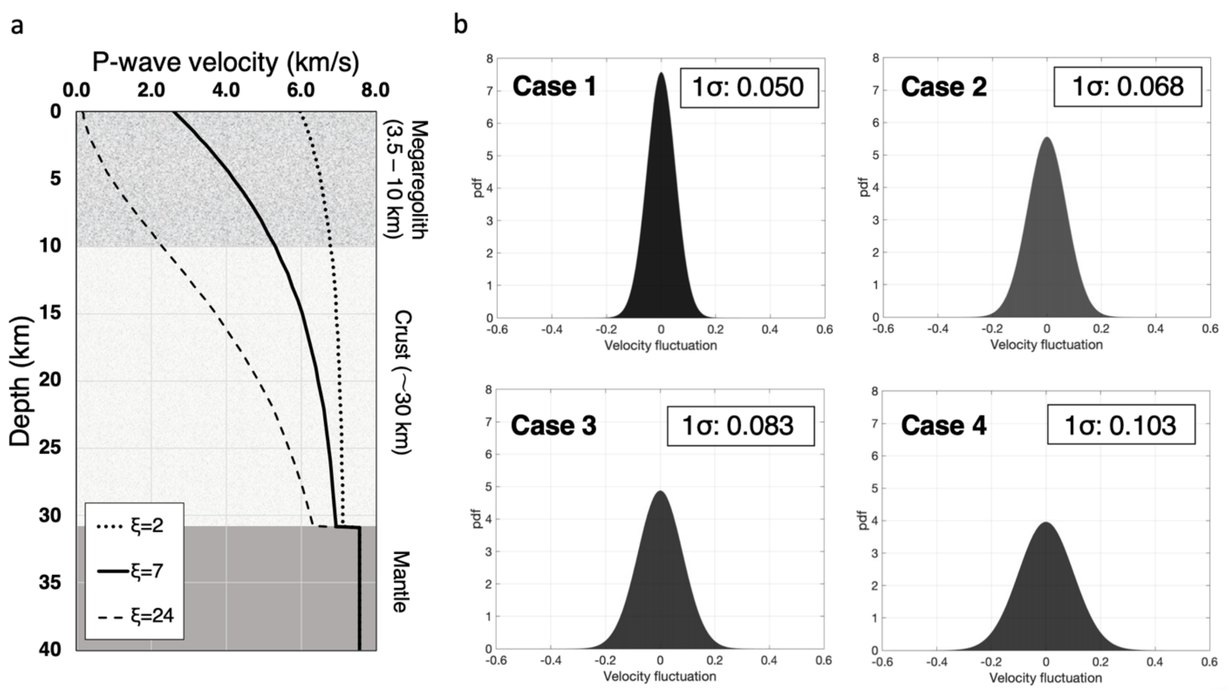

Figure 3. (a) Assumed velocity structure for the simulations. ξ=7 was employed in this work. The structure consists of three parts: megaregolith, crust, and mantle. The random media is inserted into the megaregolith layer. The thickness of the layer varied from 3.5 to 10 km in the simulation. (b) Probability density distribution of the velocity fluctuation of the representative random media used in this study. As the 1σ of the fluctuation gets larger, the scattering effect becomes stronger.

2.4 Scattering model

In terrestrial seismology, the behaviors of seismic scattering have been measured by both laboratory experiments and data analyses of seismic signals (e.g., Sato and Fehler, 1998; Sivaji et al., 2002; Sato et al., 2012). To quantitatively evaluate the properties of seismic scattering due to the heterogeneity inside a medium, previous works investigated the distribution of perturbation from an average velocity and expressed it in a mathematical way using the autocorrelation function (ACF) or power spectral density function (PSDF) (e.g., Shiomi et al., 1997; Sato and Fehler, 1998). According to Sato et al. (2012), there are a few types of ACFs: Gaussian, von Karman, and Exponential. Among these, von Karman or Exponential is usually adopted in the seismological approaches (e.g., Shiomi et al., 1997; Suzuki et al., 1981; Sivaji et al., 2002). We assumed exponential ACF (which is a specific case of von Karman ACF). It is defined as:

$$R(r) = \varepsilon^2 \exp\left(-\frac{r}{a}\right) \qquad (5)$$

where r is lag distance, a is correlation length — the characteristic scale of the heterogeneity within a certain medium, and ε is fractional fluctuation which determines the velocity perturbation from the mean velocity structure.

To simulate the megaregolith (i.e., fragmented rocks by meteoroid impacts), we assumed the isotropic random media, where the correlation length in each direction takes the same value (i.e., $a_x = a_y = a_z$), and varied the fractional fluctuation ε from 0.024 to 0.042, corresponding to the 1σ of the velocity fluctuation from 5 to 10%.

Here we focus on the four cases, where the typical scale of random media is fixed to 650 m and 1σ of the velocity fluctuation ranges from 5 to 10% (Figure 3b). The larger perturbation corresponds to more intense scattering (i.e., the scattering effects get stronger from Case 1 to Case 4). The parameter study about the correlation length is presented in Text S4.

Note that these are the parameters for the initial runs to find preferable settings before the further detailed constraints. The additional scattering structure is presented in Section 3.3.

2.5 Source model

As a source model for impacts, there are two approximations; one is the isotropic radiation with moment tensor and the other is the point force (or body force) expressed with the impulse. In past studies, either model was used to simulate the impact-induced seismic waves (e.g., Blanchette-Guertin et al., 2015; Daubar et al., 2020; Onodera et al., 2021). Since the detailed description of the impacts in terms of seismic source modeling is still an open issue, we employed the simplest model — isotropic radiation. In fact, under the intense scattering structure as considered in this study, the radiation information is lost just after the energy is released and the difference in the source model does not so much affect the resultant waveform (i.e., the structure is much more dominant to characterize the seismogram in this case). Readers can find more details in Onodera et al. (2021) for the source assumption.

It is worth noting that, through the subsequent simulations, we found that $(1.5 \pm 0.5) \times 10^{12}$ Nm is preferable as the seismic moment, which is equivalent to the seismic energy of $(5.5 \pm 1.8) \times 10^{6}$ J following Teanby and Wookey (2011). This leads to the seismic efficiency of $(1.2 \pm 0.4)\times 10^{-4}$. Because this is one of the least constrained parameters, we leave a brief note here for future impact physics works.

2.6 Quantitative comparison between synthetics and Apollo data

2.6.1 Preprocessing

First, as generally done in the seismological analysis, a long-term trend is removed from the raw Apollo seismic data. Concerning pre-filtering, the 4-th order Butterworth filter is applied with the cut-off frequency being 0.05 and 3.0 Hz. After that, we applied the Tukey window function with the lobe width being 3% of the data length. Then, the instrumental response of the Apollo LP peaked mode was corrected, which gave us the velocity time series data. After that, we performed the post-bandpass filtering around the peak sensitivity of the LP sensor in peaked mode ($0.3 - 1.5$ Hz).

Because of the radio-tracking of the artificial impacts, the source locations are well-constrained (Table S2 and S3), which enables us to obtain the radial and transverse components using the azimuth information. Note that the seismometer was not aligned in the usual way for Apollo 12, that is, the positive direction of LPX is oriented towards 180°N and that of LPY is towards 270°E.

2.6.2 Estimation of rise-time

As pointed out by Gillet et al. (2017) and Onodera et al. (2021), the first rise-coda (i.e., from the first arrival to peak energy arrival) contains the information of the forward scattering while the decay-coda (i.e., from the peak energy to noise floor) more reflects the diffusion and intrinsic attenuation factors. Since this study focuses on the forward scattering effects, we paid closer attention to the rise-coda part. In the following analysis, a parameter called "rise-time"—the time to reach the energy peak from the first arrival—is mainly used. As P or S arrival reading, the rise-time is determined manually (e.g., Onodera et al., 2021). In the case of the Moon, it is estimated by taking a moving average of the seismic records and detecting the point where the gradient of energy increase becomes flat. In this work, all the seismic signals were smoothed with a window of 200 data points (~30 s). That basically means the uncertainty of the rise-time corresponds to ±15 s.

2.6.3 Equivalent energy density

We looked into the envelope shape in order to track the energy trend in time, which helps us assess how identical the synthetic data are compared to the real one. The seismic energy is proportional to the squared amplitude. Thereby, the equivalent energy E_{eq} is given by:

$$E_{eqi} = \sum V_i^2(t) \quad (i = R, T, Z) \qquad (6)$$

where $V(t)$ is the time-series of velocity signal for the radial, transverse, and vertical components. Since this study aims to see how the energy develops with time, we divided the time series into some sections and evaluate the energy density in a certain section instead of computing the total energy. Here, we introduce a new parameter called "equivalent energy density (EED)" E_d defined as:

$$E_{d_j} = \frac{1}{\tau_{j+1}-\tau_j} \sum_{t=\tau_{j+1}}^{\tau_{j+1}} V_i^2(t) \quad (i = Z, R, T; j = 1, 2, \dots, 2N_{div} - 1) \qquad (7)$$

$$\tau_n = \frac{nT_{rise}}{N_{div}} \ (n = 1,2, \dots, 2N_{div})$$

where T_{rise} shows the rise-time, and N_{div} (=10 in this study) determines how many sections the time-series is divided into. Thereby, the E_d tells us how much energy is received at a station for a certain period, which is useful to track how the energy develops with time.

2.6.4 Amplitude ratio

As another quantitative criterion, we evaluated how much the amplitude at the rise-time A_{rise} differs from the mean amplitude A_{ave}. Figure 4 shows two different cases. The typical lunar seismic signal represents a relatively flat feature after reaching the rise-time, which results in the A_{rise}/A_{ave} ratio of ~1.4 (Figure 4a). Note that the time window between the first arrival and $2T_{rise}$ is used to compute the average value. On the other hand, if a signal has a strong peak as in Figure 4b, the ratio takes a higher value.

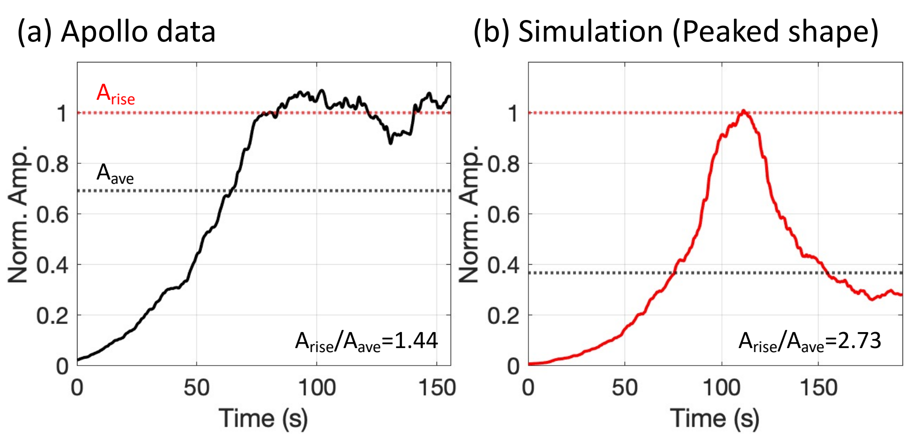

Figure 4. Examples of the amplitude ratio for (a) Apollo data and (b) simulation (Case1). A_{rise} is the amplitude at the rise-time, and A_{ave} stands for the average amplitude between arrival to $2T_{rise}$.

3 Evaluation of scattering property around the Apollo 12 landing site

As only two events are available in this study, the procedure goes like: (1) constraining the scattering structure for the closer event (Apollo 16 SIVB impact), then (2) applying the structure to another event (Apollo 14 SIVB impact) to see whether the same structure can explain both observations. Unless the structure worked well for two events, a revision in the scattering structure would be given to minimize the discrepancy between synthetics and the data. Section 3.1 shows the results of rise-time, energy trend, and envelope shape for Apollo 16 SIVB impact observed at Station 12. Section 3.2 explains whether the structure based on the Apollo 16 SIVB event also works for Apollo 14 SIVB, and Section 3.3 describes how to improve the scattering structure to better explain both events.

3.1 The initial simulation results for Apollo 16 SIVB impact

Some examples of the simulation outputs are displayed in Figure 5 including snapshots of the horizontal plane (Figure 5a) and the comparison of smoothed energy envelopes for the radial component between the Apollo (black profile) and synthetics (colored profile) (Figure 5b). The snapshots show the time development of wave propagation where the red wave shows the compressional component and the green does the shear component. The black circle pattern corresponds to the Rayleigh wave (e.g., the second panel in the first row of Figure 5a), which cannot be confirmed in the Apollo data. Thus, one of the important constraints in reproducing the Apollo observation is to attenuate the Rayleigh wave energy to the level of scattered body wave energy. Comparing the four scattering models, it is obvious that the stronger scattering (e.g., Case 4) diffuses the Rayleigh wave energy more rapidly compared to the weaker ones (e.g., Case 1) (Figure 5a). This difference can also be seen in the synthetic waves (Figure 5b). While the synthetic envelope shows a strong peak of the Rayleigh wave in the weak scattering condition (Case 1), as the scattering becomes more intense (Case 4), the surface wave energy is attenuated and the envelope shape gets more similar to the observation.

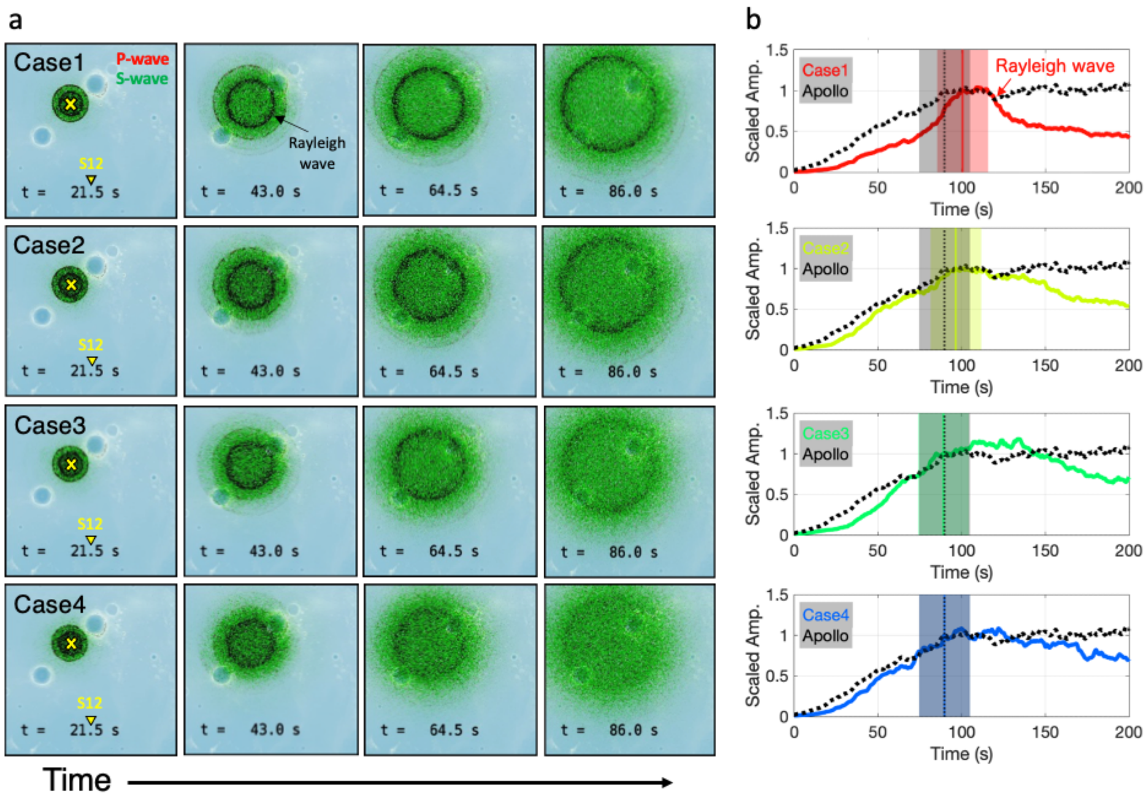

Figure 5. (a) Snapshots of each simulation on the horizontal plane. The time developments of wave propagation for Case 1 through Case 4 are shown from the top to bottom row. The yellow cross shows the location of the source (Apollo 16 SIVB impact) and the seismic station (Station 12). The red wave corresponds to the compressional component and the green to the shear component. In this case, the random media displayed in Figure 3b are inserted in the first 5 km. (b) Comparison of smoothed envelopes of the radial component between the Apollo and synthetics for the respective cases. All results are filtered between 0.3 – 1.5 Hz, then smoothed with a 30 s time window and 50% overlap. The black curve corresponds to the Apollo data and the colored ones to the synthetics for Case 1 through Case 4 from the top to bottom. The vertical lines with shade represent the peak energy (rise-time) arrivals and their error ranges. The error bar follows the window size for smoothing. The amplitudes are normalized with the value at the respective rise-times.

More quantitative comparison between the observations and synthetics was made by measuring the rise-time and EED (Figure 6a-c). While Case 1 and 2 are plotted far away from the Apollo, the intense scattering cases (Case 3 and 4) are in accordance with the observation. Moreover, looking at the results of the amplitude ratio (Figure 6d), we clearly observe that the ratio gets closer to the observation as the scattering gets stronger – meaning that the envelop shape changes from peaked-shape to flat one as seen in Figure 5b. From these results, we conclude Case 4 is preferable as a base model for the further investigations in the following sections.

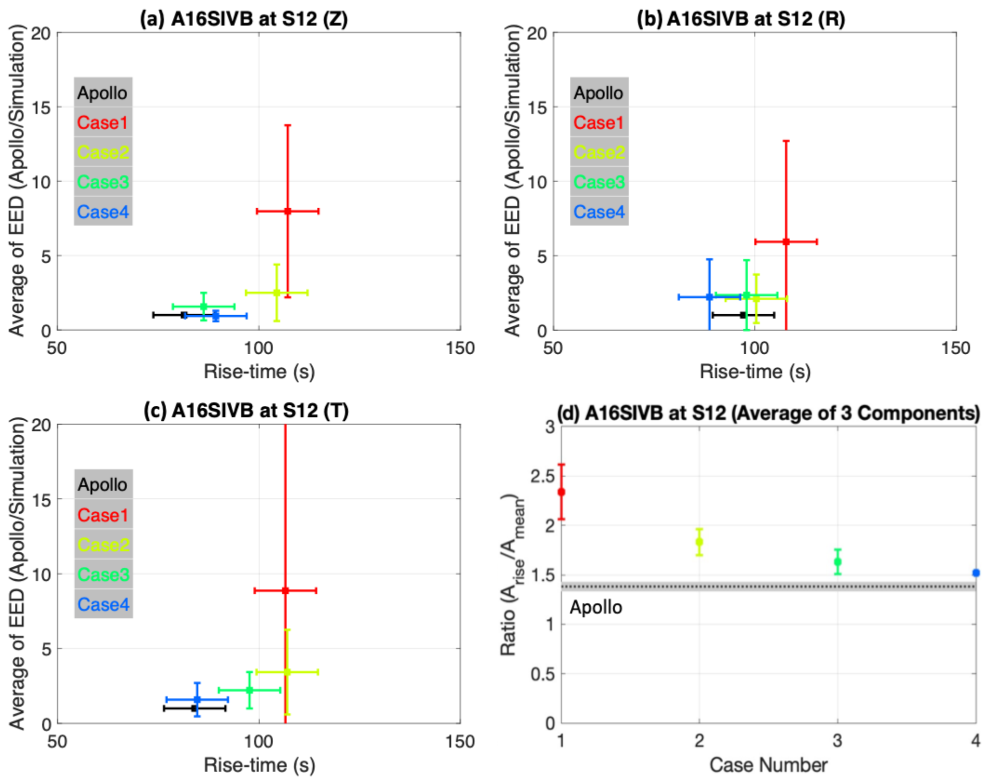

Figure 6. Rise-time versus equivalent energy density ratio (EED ratio) for (a) the vertical, (b) the radial, and (c) the transverse components. The black plots show the Apollo, and the colored are for respective simulation cases. The horizontal axis shows the rise-time with error of 15 s. The vertical axis shows the average value of the EED ratio between the observation and synthetics over $2T_{rise}$ with standard deviation. (d) Results of the amplitude ratio values. The colored plots with error bars show the averaged values of the vertical, radial, and transverse components. The black dotted lines are the amplitude ratio values for the Apollo data with error range.

3.2 Application of the estimated scattering model to Apollo 14 SIVB impact

To observe whether Case 4 — the best model for Apollo 16 SIVB impact — can also explain the other event, we performed another simulation for the Apollo 14 SIVB impact under the same parameter settings. Figure 7 compares the simulated envelopes with the Apollo ones. Overall, the envelope shape shows similar features to the data. The rise-time is in accordance with the error range for all components, and the amplitude ratio averaged using the three components takes the value of 1.59 ± 0.10 close to that of the Apollo (1.30 ± 0.05). However, making a comparison with the Case 4 results for the Apollo 16 SIVB impact (i.e., Figure 5b and Figure 7b), it does not seem that the fitting and the consistency of rise-time is as good as that for the Apollo 16 SIVB case. In the following section, we give some modifications to the Case 4 structure to see what kind of model can improve the results.

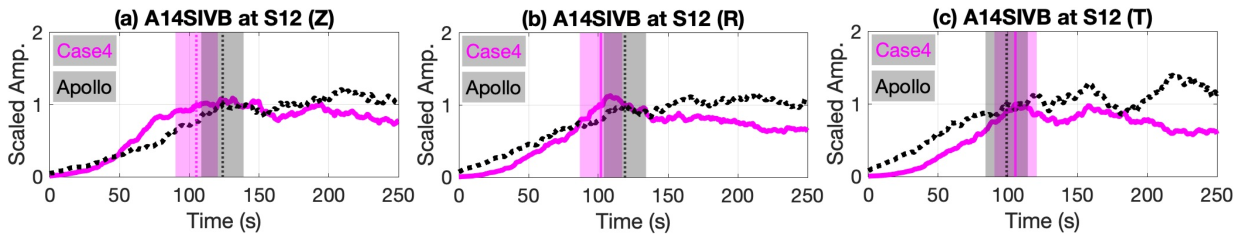

Figure 7. Smoothed envelopes of Apollo 14 SIVB impact observed at Station 12 in (a) the vertical, (b) the radial, and (c) the transverse components. The black envelopes are for the Apollo data, and the magenta profiles are for the simulation assuming Case 4 structure. The vertical lines with shade show the rise-time arrivals with error ranges. All envelopes are normalized with the value at each rise-time.

3.3 Modification of the vertical scattering structure

To improve the simulation results for Apollo 14 SIVB impact case, we modify the vertical scattering structure. Since the computation is expensive (28 TB total memory for each run), we prepared three different structures to roughly confirm what kind of structure improves the synthetics. The assumed structures (Case 4α, β, and γ) are shown in Figure 8a. Among these models, Case 4α shows a gradual decrease in velocity fluctuation. In Case 4β, the scattering gets rapidly weak at 3.5 km (i.e., thin intense scattering). Case 4γ keeps the intense scattering layer down to 10 km, then rapidly turns into a consolidated structure below that depth.

The simulation results are displayed in Figure 8b-d. Looking at the vertical components, there is little difference between the three cases. On the other hand, some differences can be confirmed in the horizontal components. For example, while the rise-times of Case 4β and γ (blue and green) coincide with the data within the error bars, the transverse component of Case 4α (red) does not. From the comparison between Case 4α with the rest of the two, it does not seem that the gradually changing structure is suitable for the Apollo 12 landing site.

Concerning the preference between the thin (Case 4β) or the thick scattering layer (Case 4γ), Case 4γ is more similar to the observation, which can be confirmed from the averaged amplitude ratio in Figure 9. In fact, Case 4γ also works well for Apollo 16 SIVB impact (Figure 10). Thus, the intense scattering appears to continue down to 10 km at least at the Apollo 12 landing site.

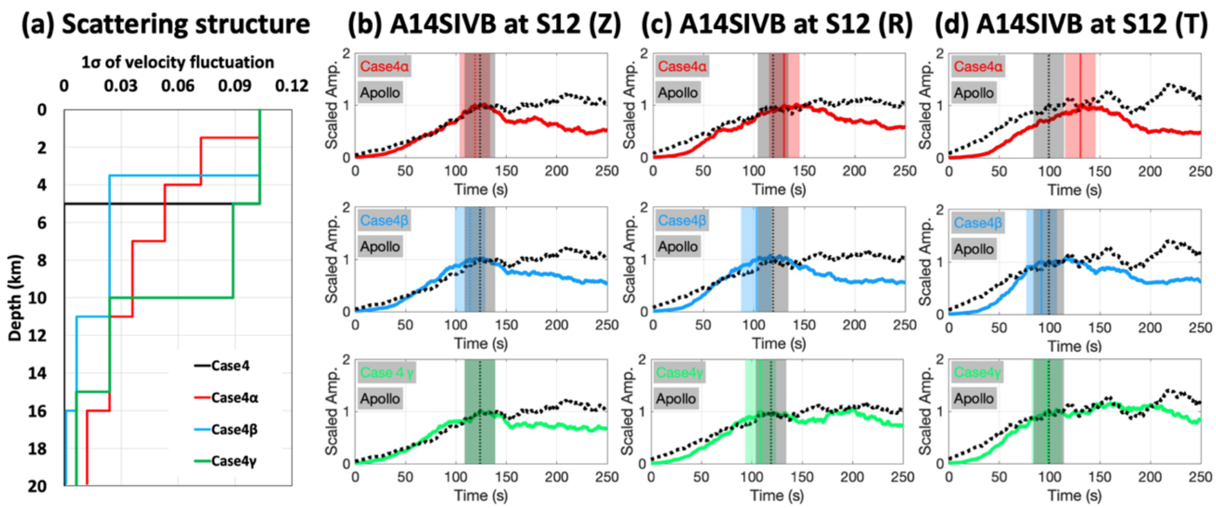

Figure 8. (a) Assumed scattering structures. The black line is Case 4 which was used in the previous section. The red, blue, and green are Case 4α, β, γ, respectively. (b)-(d) The comparisons between the simulation results (colored) with the Apollo data (black) for the vertical, radial, and transverse components from left to right. The first row is for Case 4α, followed by Case 4β, and Case 4γ. The vertical lines with shade represent the rise-times with their error ranges.

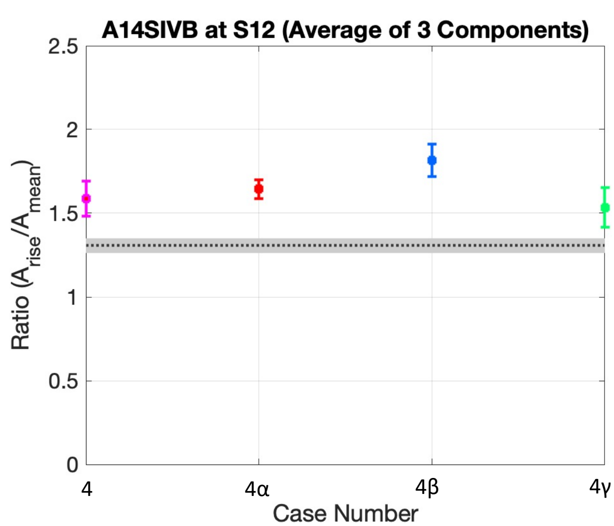

Figure 9. Averaged amplitude ratios of the three components. Magenta plot is for Case 4, red for Case 4α, blue for Case 4β, and green for Case 4γ.

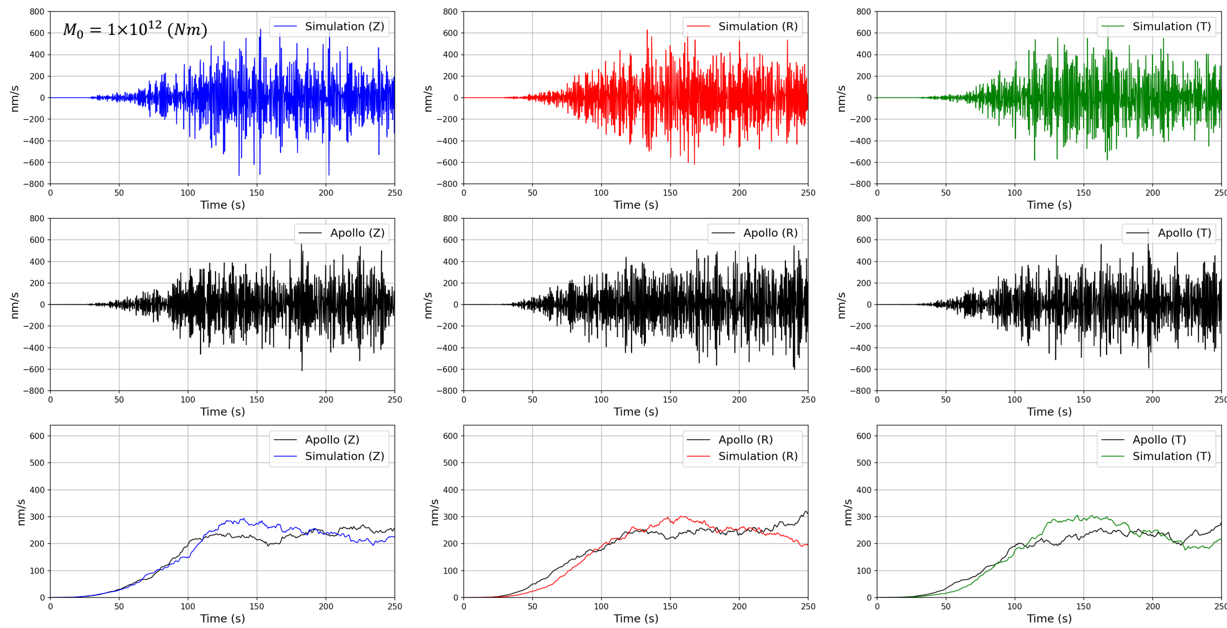

Figure 10. The results for Apollo 16 SIVB impact for Case 4 γ. (Top row) Simulated waveforms in nm/s. The vertical, radial, and transverse components are shown from the left to right. The waveforms are filtered between 0.3 and 1.5 Hz. (Middle row) The vertical, radial, and transverse waveforms of the Apollo data from the left to right. The same filter is applied to the respective data as that of the simulation. (Bottom row) Comparisons of smoothed envelopes between the Apollo (black) and the simulation (colored).

4 Discussion

4.1 Interpretation of the derived structure

From the forward modeling, we found that the 10 km intense scattering model (Case 4γ) best explains the observations. The structural transition at 10 km depth was actually expected in previously proposed models (Hawke et al., 2003; Yamamoto et al., 2012), although that is more related to the compositional transition from the mafic-rich materials into the plagioclase-rich anorthosite. It is also pointed out that the mafic-rich layer has compositional variations due to the continuous meteoroid impacts in the early history of the Moon (Hawke et al., 2003).

On the other hand, the numerical simulation of the spatial development of impact fragments by Wiggins et al. (2019) showed that the fragmentations with several hundreds of meters, which affect the seismic wave propagation, could develop down to 5 km from the surface. Putting together these pieces of information with our model, within the 10 km scattering layer, the first several-km layer reflects the structural fragmentation and more reflects the compositional variations below that; then the structure turns into a massive plagioclase-rich crust where the composition and physical structure get more homogeneous at around 10 km depths.

4.2 Comparison between the Earth, Mars, and the Moon in terms of scattering and attenuation environment

The quantified scattering parameter enables us to compare the scattering environment between the Earth, Mars, and the Moon. Figure 11a compares the three solid bodies from the viewpoint of seismic scattering, where the intensity of scattering is evaluated with scattering attenuation factor Q_s defined as:

$$Q_s^{-1} = \frac{n_s}{k_s} \qquad (8)$$

where n_s is the scattering coefficient corresponding to the reciprocal of the mean free path between scattering media. Here, we regarded the correlation length as the mean free path. k_s is wavenumber for a given frequency, that is:

$$k_s = \frac{2\pi f}{V} \qquad (9)$$

where f refers to the frequency —ranging from 0.3 to 1.5 Hz—and V is the seismic wave velocity (S-wave velocity in the megaregolith layer in this study). The smaller Q_s value (i.e., larger Q_s^{-1}) means more intense scattering. In Figure 11a, the lunar and Martian Q_s (colored filled area) are superposed on those evaluated at various sites on the Earth (Sato et al., 2012 and references therein).

Paying attention to the terrestrial Q_s^{-1}, it ranges from 10^{-1} to 10^{-5} in the lithosphere and does from 5×10^{-3} to 10^{-4} in the mantle. The volcanic region, whose subsurface structure is heterogenous, shows a relatively high value of 10^{-2} compared to the typical values for the lithosphere. Turning to Mars, the first results from the InSight (Interior Exploration using Seismic Investigations, Geodesy and Heat Transport) mission (Menina et al., 2021) shows a similar value to those observed in the terrestrial lithosphere. Two filled areas are displayed for the Moon: one is estimated based on the radiative transfer modeling (Gillet et al., 2017) and the other is through the numerical simulation done in this study. Gillet et al. (2017)

analyzed various types of moonquakes besides meteoroid impacts whose excited waves are sensitive to the subsurface heterogeneity) and estimated the global structure of Q_s (the crustal value is presented in Figure 11a). On the contrary, our research focuses on the closely located impacts, which are suitable for investigating megaregolith — the most heterogeneous region on the Moon. While the lunar crustal Q_s^{-1} is comparable with the most inhomogeneous region on the Earth displayed, the lunar megaregolith Q_s^{-1} shows a higher value than those measured on the Earth and Elysium Planitia on Mars, suggesting the uppermost part of the Moon is highly heterogeneous.

Our results arise a question; why does the Moon show more intense scattering than others? The answer can be explained by the difference in gravity conditions. It is known that the compressional pressure increases more rapidly under larger gravity conditions. In other words, the critical depth — where the plastic deformation stops — is located shallower as the planet's size gets larger, making it harder for impact fragments to develop (Wiggins et al., 2019). In addition, the existence of an atmosphere plays an important role in the surface evolution of a solid body. With an atmosphere, the impact velocity would be decelerated, resulting in smaller impact energy. Thus, it is reasonable that the Moon has a much more heterogeneous structure because of its smaller size and the lack of an air shield against continuous meteoroid impacts over several billion years.

Another comparison is made in Figure 11b where the intrinsic attenuation factor Q_i is compared between the three bodies. The smaller Q_i (i.e., larger Q_i^{-1}) indicates that the seismic energy attenuates more rapidly, generally implying that the medium includes more fluid. On Earth, large Q_i^{-1} ($\sim 10^{-2}$) is obtained at geologically active regions (e.g., volcanic front, active fault) (e.g., Sato et al., 2012). In the case of the Moon and Mars, much lower Q_i^{-1} values are obtained, indicating they are in an extremely dry environment, especially compared to the terrestrial lithosphere. This is consistent with a general view of the respective planetary environments. Combining these facts with Q_s results makes it easier to interpret the differences in the seismic observations on each body. Since the Moon is in extremely heterogenous and low attenuation conditions, the seismic waves are highly scattered with less absorption, making the seismic phases unclear and prolonging the event duration. Mars shows a dry environment, but the scattering factor is comparable with that of the Earth's lithosphere. This explains why marsquakes have a longer duration than those on Earth with less diffused phase arrivals (such as P, S) than moonquakes (Lognonné et al., 2020).

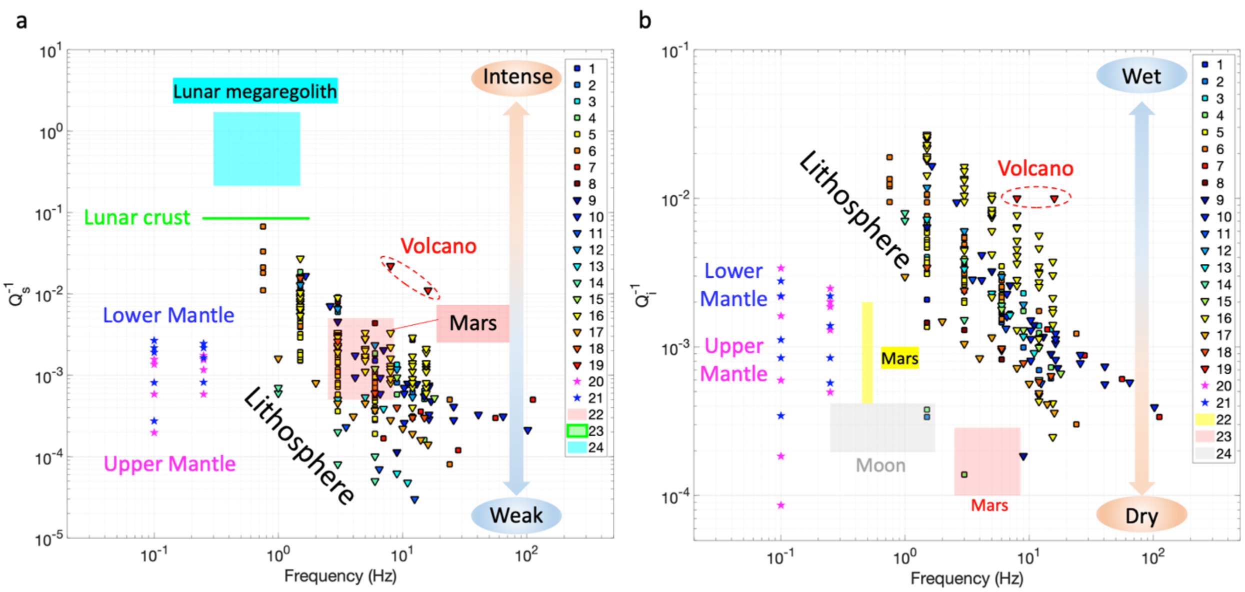

Figure 11. (a) Comparison of scattering attenuation factor between the Earth, Mars, and the Moon. The horizontal axis shows frequency and the vertical shows the inverse value of the scattering attenuation factor. The larger Q_s^{-1} shows the more intense scattering. For the terrestrial case, results for a variety of areas are plotted. The red hatched area is the first result of Elysium Planitia on Mars in the InSight mission. The green-filled area shows the previous estimate for the lunar crust and the cyan area shows our result for the lunar megaregolith. The numbers in the legend correspond to the references summarized in Table S6. (b) Comparison of intrinsic attenuation factor between the Earth, Mars, and the Moon. The larger Q_i^{-1} shows the larger attenuation, implying that the medium holds more fluid. As in (a), the results for various fields on the Earth and Elysium Planitia on Mars, the crust, and/or mantle of the Moon are shown together. The numbers in the legend correspond to the references summarized in Table S7.

5 Conclusions

In this study, we accomplished the first reproduction of the intensely scattered seismic waves observed on the Moon through the full 3D seismic wave propagation simulation. This allowed us to make significant progress in understandings of scattering properties of the most heterogeneous region of the Moon (megaregolith), which has been a long-standing problem since lunar seismology started.

The quantified scattering parameters are compared with those evaluated on other planets, helping us interpret the different characteristics observed in seismic waves on each solid body. Since the seismic scattering is a common feature seen in planetary seismology, our approach would be helpful in investigating any other solid planetary bodies in future explorations.

To summarize, our study not just shed light on one of the most complicated problems in lunar seismology but also opened a new way for comparative planetology in terms of seismic scattering, which is expected to give us a paramount key to further understanding of how a planetary surface evolved since its formation.

Acknowledgments

We appreciate Japan Agency for Marine-Earth Science and Technology (JAMSTEC) for providing us with computational resources (the Earth Simulator). We thank Dr. Makiko Ohtake of University of Aizu and Dr. Hiroshi Nagaoka of RIKEN for giving us constructive advice from the viewpoint of the geochemical evolution of the Moon.

Data Availability

The Apollo seismic data used in this study were collected from the Data Archives and Transmission System (DARTS) by the Center for Science-satellite Operation and Data Archive (C-SODA) of the Institute of Space and Astronautical Science of the Japan Aerospace Exploration Agency (https://darts.isas.jaxa.jp/ planet/seismology/apollo/index.html). Simulation outputs are available at Onodera (2022). The maps were made with the Generic Mapping Tool (GMT; Wessel et al., 2019).

References

- Araki, H., Tazawa, S., Noda, H., Ishihara, Y., Goossens, S., Sasaki, S. et al. (2009), Lunar Global Shape and Polar Topography Derived from Kaguya-LALT Laser Altimetry, *Science*, 323, 897-900, https://www.science.org/doi/10.1126/science.1164146.

- Barker, M. K., Mazarico, E., Neumann, G. A., Zuber, M. T., Haruyama, J., Smith, D. E. (2016), A new lunar digital elevation model from the lunar orbiter laser altimeter and SELENE terrain camera, *Icarus, 273*, 346-355, https://doi.org/10.1016/j.icarus.2015.07.039.
- Besserer, J., Nimmo, F., Wieczorek, M. A., Weber, R. C., Kiefer, W. S., McGovern, P. J., Andrews-Hanna, J. C., Smith, D. E., and Zuber, M. T. (2014), GRAIL gravity constraints on the vertical and lateral density structure of the lunar crust, *Geophys. Res. Lett.*, 41, 5771– 5777, doi:10.1002/2014GL060240.
- Dainty, A. M. and Toksöz, M., N. (1981), Seismic coda on the Earth and the Moon: a comparison, *Phys. Earth Planet. Int., 26*, 250-260, https://doi.org/10.1016/0031-9201(81)90029-7.
- Garcia, R.F., Khan, A., Drilleau, M. *et al*. Lunar Seismology: An Update on Interior Structure Models. *Space Sci Rev* **215,** 50 (2019). https://doi.org/10.1007/s11214-019-0613-y.
- Gillet, K., Margerin, L., Calvet, M., Monnereau, M. (2017), Scattering attenuation profile of the Moon: implications for shallow moonquakes and the structure of the megaregolith, *Phys. Earth Plant. Int., 262*, 28-40, https://doi.org/10.1016/j.pepi.2016.11.001.
- Hawke, B. R., Peterson, C. A., Blewett et al. (2003), Distribution and modes of occurrence of lunar anorthosite, *J. Geophys. Res.*, 108, 5050, doi:10.1029/2002JE001890, E6.
- Latham, G. et al. (1970), Seismic data from man-made impacts on the Moon, *Science, 170*, 3958, 620-626, doi: 10.1126/science.170.3958.620.
- Lognonné, P., Banerdt, W.B., Pike, W.T. *et al*. (2020), Constraints on the shallow elastic and anelastic structure of Mars from InSight seismic data. *Nat. Geosci*. **13,** 213–220, https://doi.org/10.1038/s41561-020-0536-y.
- Maeda, T., Takemura, S. & Furumura, T. (2017). OpenSWPC: an open-source integrated parallel simulation code for modeling seismic wave propagation in 3D heterogeneous viscoelastic media. *Earth Planets Space* **69,** 102, https://doi.org/10.1186/s40623-017-0687-2.

- Menina, S., Margerin, L., Kawamura, T., Lognonné, P., Marti, J. et al. (2021), Energy envelope and attenuation characteristics of high frequency (HF) and very-high-frequency (VF) Martian events, *Bull, Seismol. Soc. Am., 111*, 6, 3016–3034, https://doi.org/10.1785/0120210127.
- Nakamura, T., Takenaka, H., Okamoto, T., Kaneda, Y. (2012), FDM simulation of seismic-wave prop- agation for an aftershock of the 2009 Suruga bay earthquake: effects of ocean-bottom topography and seawater layer, *Bull. Seismol. Soc. Am., 102*, 2420-2435, https://doi.org/10.1785/0120110356.
- Oberst, P. J. (1989), Meteoroids near the Earth-Moon system as inferred from temporal and spatial distribution of impacts detected by the lunar seismic network, PhD dissertation, The University of Texas at Austin.
- Onodera, K., Kawamura, T., Tanaka, S., Ishihara, Y., and Maeda, T. (2021). Numerical simulation of lunar seismic wave propagation: Investigation of subsurface scattering properties near Apollo 12 landing site. *Journal of Geophysical Research: Planets*, 126, e2020JE006406. https://doi.org/10.1029/2020JE006406.
- Onodera (2022), Onodera0726/JGR_Onodera_2023, GitHub Data Repository, https://github.com/Onodera0726/JGR_Onodera_2022.git.
- Sato, H. and Fehler, M. (1998) Seismic wave propagation and scattering in the heterogeneous Earth, AIP Press/Springer, New York.
- Sato, H., Fehler, M. C., Maeda, T. (2012), Seismic wave propagation and scattering in the heterogeneous Earth, *2nd edn*, Springer, Berlin.
- Shiomi, K., Sato, H., Ohtake, M. (1997) Broad-band power-law spectra of well-log data in Japan, *Geophys. J. Int., 130*, 57–64, https://doi.org/10.1111/j.1365-246X.1997.tb00987.x.
- Sondergeld, C. H., Granryd, L. A., Spetzler, H. A. (1979), Compressional velocity measurements for a highly fractured lunar anorthosite, *Prc. Lunar Planet. Sci. Conf., 10th*, 2147-2154.

- Wessel, P., Luis, J. F., Uieda, L., Scharroo, R., Wobbe, F., Smith, W. H. F., & Tian, D. (2019). The Generic Mapping Tools version 6. *Geochemistry, Geophysics, Geosystems*, 20, 5556– 5564. https://doi.org/10.1029/2019GC008515.
- Wieczorek, M. A., Neumann, G. A., Nimmo, F., Kiefer, W. R., Taylor, G. J., Melosh, H. J., The crust of the Moon as seen by GRAIL, *Science*, *339*, 6120, 671-675, DOI: 10.1126/science.1231530.
- Wiggins, S. E., Johnson, B. C., Bowling, T. J., Melosh, H. J., & Silber, E. A. (2019). Impact fragmentation and the development of the deep lunar megaregolith. *Journal of Geophysical Research: Planets*, 124, 941– 957. https://doi.org/10.1029/2018JE005757.
- Yamamoto, S., Nakamura, R., Matsunaga et al. (2012), Massive layer of pure anorthosite on the Moon, *Geophys. Res. Lett.*, 39, L13201, doi:10.1029/2012GL052098.

References from the Supporting Information

- Adams, D.A. and Abercrombie, R.E. (1998), Seismic attenuation above 10 Hz in southern California from coda waves recorded in the Cajon Pass borehole, *J. Geophys. Res.*, 103:24, 257–24, 270, https://doi.org/10.1029/98JB01757.
- Akinci, A, Pezzo, E.D., Ibanez, J.M. (1995), Separation of scattering and intrinsic attenuation in southern Spain and western Anatolia (Turkey), *Geophys. J. Int.*, 121:337–353, https://doi.org/10.1111/j.1365-246X.1995.tb05715.x.
- Akinci, A. and Eyidogan, H. (2000), Scattering and anelastic attenuation of seismic energy in the vicinity of north Anatolian fault zone, eastern Turkey, *Phys. Earth Planet. Inter.*, 122:229–239, https://doi.org/10.1016/S0031-9201(00)00196-5.
- Bianco, F., Pezzo, E.D., Castellano, M., Ibanez, J., Luccio, F.D. (2002), Separation of intrinsic and scat- tering seismic attenuation in the Southern Apennine zone, Italy, *Geophys. J. Int.*, 150(1):10–22, https://doi.org/10.1046/j.1365-246X.2002.01696.x.

- Bianco, F., Pezzo, E.D., Malagnini, L., Luccio, F.D., Akinci, A. (2005), Separation of depth-dependent intrinsic and scattering seismic attenuation in the northeastern sector of the Italian Peninsula. *Geophys. J. Int.*, 161(1):130–142, https://doi.org/10.1111/j.1365-246X.2005.02555.x.
- Blanchette-Guertin, J.-F., Johnson, C. L., and Lawrence, J. F. (2012), Investigation of scattering in lunar seismic coda, *J. Geophys. Res.*, 117, E06003, doi:10.1029/2011JE004042.
- Blanchette-Guertin, J. F., Johnson, C. L., and Lawrence, J. F. (2015), Modeling seismic energy propagation in highly scattering environments. *J. Geophys. Res. Planets*, 120, 515– 537. doi: 10.1002/2014JE004654.
- Daubar, I. J., Lognonné, P., Teanby, N. A., Collins, G. S., Clinton, J., Stahler, S. et al. (2020), A new crater near InSight: Implications for seismic impact detectability on Mars, *J. Geophys. Res.: Planets*, 125, e2020JE006382, https://doi.org/10.1029/2020JE006382.
- Dutta, U., Biswas, N., Adams, D., Papageorgiou, A. (2004), Analysis of S-wave attenuation in South- Central Alaska, *Bull. Seism. Soc. Am.*, 94(1):16–28, https://doi.org/10.1785/0120030072.
- Fehler, M., Hoshiba, M., Sato, H., Obara, K. (1992), Separation of scattering and intrinsic attenuation for the Kanto-Tokai region, Japan, using measurements of S-wave energy versus hypocentral distance, *Geophys. J. Int.*, 108:787–800, https://doi.org/10.1111/j.1365-246X.1992.tb03470.x.
- Garcia, R. F., Gagnepain-Beyneix, J., Chevrot, S., Lognonné, P. (2011), Very preliminary reference Moon model, *Phys. Earth Planet. Int., 188*, 96-113, https://doi.org/10.1016/j.pepi.2011.06.015.
- Giampiccolo, E., Tuve, T., Gresta, S., Patane, D. (2006), S-waves attenuation and separation of scattering and intrinsic absorption of seismic energy in southeastern Sicily (Italy), *Geophys. J. Int.*, 165:211–222, https://doi.org/10.1111/j.1365-246X.2006.02881.x.
- Goutbeek, F.H., Dost, B., van Eck, T. (2004), Intrinsic absorption and scattering attenuation in the southern part of the Netherlands, *J. Seis.*, 8:11–23, https://doi.org/10.1023/B:JOSE.0000009511.27033.79.

- Hatzidimitriou, P.M. (1994), Scattering and anelastic attenuation of seismic energy in northern Greece, *Pure Appl. Geophys.*, 143:587–601, https://doi.org/10.1007/BF00879499.
- Hoshiba, M. (1993), Separation of scattering attenuation and intrinsic absorption in Japan using the multiple lapse time window analysis of full seismogram envelope, *J. Geophys. Res.*, 98 (B9), 15809– 15824, doi:10.1029/93JB00347.
- Jin, A., Mayeda, K., Adams, D., and Aki, K. (1994), Separation of intrinsic and scattering attenuation in southern California using TERRAscope data, *J. Geophys. Res.*, 99(B9), 17835– 17848, doi:10.1029/94JB01468.
- Leary, P. and Abercrombie, R. (1994), Frequency dependent crustal scattering and absorption at 5−160 Hz from coda decay observed at 2.5 km depth, *Geophys. Res. Lett.*, 21:971–974, https://doi.org/10.1029/94GL00977.
- Lee, W. S., Sato, H., and Lee, K. (2003), Estimation of *S*-wave scattering coefficient in the mantle from envelope characteristics before and after the *ScS* arrival, *Geophys. Res. Lett.*, 30, 2248, doi:10.1029/2003GL018413, 24.
- Lee, W.S., Sato, H., Lee, K. (2006), Scattering coefficients in the mantle revealed from the seismogram envelope analysis based on the multiple isotropic scattering model, *Earth Planet. Sci. Lett.*, 241:888–900, https://doi.org/10.1016/j.epsl.2005.10.035.
- Lognonné, P., Gagnepain-Beyneix, J., Chenet, H. (2003), A new seismic model of the Moon: implications for structure, thermal evolution and formation of the Moon, *Earth Plant. Sci. Lett., 211*, 27-44, https://doi.org/10.1016/S0012-821X(03)00172-9.
- Mayeda, K., Koyanagi, S., Hoshiba, M., Aki, K., and Zeng, Y. (1992), A comparative study of scattering, intrinsic, and coda Q^{-1} for Hawaii, Long Valley, and central California between 1.5 and 15.0 Hz, *J. Geophys. Res.*, 97 (B5), 6643– 6659, doi:10.1029/91JB03094.
- Nakamura, Y., and Koyama, J. (1982), Seismic *Q* of the lunar upper mantle, *J. Geophys. Res.*, 87 (B6), 4855– 4861, doi:10.1029/JB087iB06p04855.
- Orloff (2000), Apollo by the numbers: a statistical reference, NASA SP-2000-4029.

- Teanby and Wookey (2011), Seismic detection of meteorite impacts on Mars, *Phys. Earth Planet. Int., 186*, 70-80, https://doi.org/10.1016/j.pepi.2011.03.004.
- Toksöz, M. N., Dainty, A. M., Solomon, S. C., and Anderson, K. R. (1974), Structure of the Moon, *Rev. Geophys.*, 12(4), 539– 567, doi:10.1029/RG012i004p00539.
- Ugalde, A., Pujades, L.G., Canas, J.A., Villasenor, A. (1998), Estimation of the intrinsic absorption and scattering attenuation in northeastern Venezuela (southeastern Caribbean) using coda waves, *Pure Appl. Geophys.*, 153:685–702, DOI: 10.1007/978-3-0348-8711-3_21.
- Vargas, C.A., Ugalde, A., Pujades, L.G., Canas, J.A. (2004), Spatial variation of coda wave attenuation in northwestern Colombia, *Geophys. J. Int.*, 158:609–624, https://doi.org/10.1111/j.1365-246X.2004.02307.x.
- Yamamoto, M., and Sato, H. (2010), Multiple scattering and mode conversion revealed by an active seismic experiment at Asama volcano, Japan, *J. Geophys. Res.*, 115, B07304, doi:10.1029/2009JB007109.
- Wagner, R. V., Nelson, D. M., Plescoa, J. B., Robinson, M. S., Speyerer, E. J., Mazarico, E. (2017), Coordinates of anthoropogenic features on the Moon, *Icarus, 283*, 92-103, https://doi.org/10.1016/j.icarus.2016.05.011.